Experimental Thermal and Fluid Science 131 (2022) 110526

Contents lists available at ScienceDirect

Experimental Thermal and Fluid Science

journal homepage: www.elsevier.com/locate/etfs

Flow pattern observations and flow pattern map for adiabatic two-phase flow of carbon dioxide in vertical upward and downward direction

David Schmid [a,b,*], Bart Verlaat [a], Paolo Petagna [a], Rémi Revellin [c,1], Jürg Schiffmann [b,1]

[a] European Organization for Nuclear Research (CERN), CH-1211 Geneva 23, Switzerland
[b] Ecole Polytechnique Fédérale de Lausanne, EPFL STI IGM LAMD, CH-2002 Neuchâtel, Switzerland
[c] Univ Lyon, INSA Lyon, CNRS, CETHIL, UMR5008, F-69621 Villeurbanne, France

ARTICLE INFO

Keywords:
Carbon dioxide (CO_2)
Flow pattern map
Vertical two-phase flow
Detector cooling in High Energy Physics
Evaporative cooling
High-speed imaging
Frame- and flow-regime classifier
R744

ABSTRACT

A test facility to investigate flow pattern transitions of vertical two-phase flow of CO_2 has been built within the scope of the high-luminosity detector upgrades at the European Organization for Nuclear Research (CERN). Adiabatic flow pattern observations for both vertical up- and downflow are recorded with high-speed imaging in tubes of 8 mm inner diameter, with saturation temperatures in the range of −25°C to +5°C and mass velocities ranging from 100 kg m^{-2} s^{-1} to 450 kg m^{-2} s^{-1}. A database of 431 flow pattern observations in upward and 123 in downward direction has been compiled. The recorded data have been analysed with machine learning techniques and a previously trained Frame- and Flow-Regime-Classifier is used for the flow regime classification. The observed two-phase flow pattern transitions did not match the transition lines of existing flow pattern maps. As a consequence, new transition lines for the bubbly-to-slug, slug-to-churn and churn-to-annular transitions have been developed for both vertical upflow and downflow respectively and condensed into new flow pattern maps. It is concluded, that the flow regime transitions are strongly depended on vapour quality, mass velocity, the flow direction and the fluid properties. Compared to horizontal flow, a dryout region is not observed and the liquid film of the annular flow regime dries out symmetrically at vapour qualities close to $x = 1$.

1. Introduction

The global warming potential (GWP) of refrigerants and their impact on climate change have been gaining considerable attention within the last decades. The need for refrigeration appliances and their cooling capacities are constantly increasing all over the world – e.g. in the fields of medical applications, data centres and experiments in High Energy Physics (HEP), to mention a few – whereas the global objectives on climate protection are becoming increasingly ambitious. One promising approach to reconcile these contradictory expectations is the replacement of synthetic with natural working fluids with a low GWP.

The European Organization for Nuclear Research (CERN) is supporting eco-friendly refrigeration technologies in its experiments, in order to reduce their environmental impact. Carbon dioxide (CO_2) has already shown good performance in several cooling applications in High Energy Physics experiments [1,2] and is, due to its beneficial thermo-physical properties, a promising candidate for replacing synthetic working fluids [3,4]. Therefore, ATLAS and CMS, the two largest experiments at the Large Hadron Collider (LHC), decided to use evaporative CO_2 cooling for the thermal management of their new inner tracking detectors, that are currently under development in the scope of the high luminosity upgrades of the LHC (HL-LHC). The power dissipation of the ATLAS Inner Tracker (ITk) and the CMS Inner Detector will be 0.3 MW and 0.5 MW respectively, while, in order to cope with the high radiation level present at the LHC, both detectors will be operated at temperatures down to −40°C [5]. Experiments in High Energy Physics are positioned far from their ancillary service systems and are typically connected to the cooling plants by long transfer lines – in the order of 100 m – with both horizontal and vertical segments. This layout, combined with the need of stable and precisely controlled operational temperatures, is particularly well suited for Two-Phase Accumulator Controlled Loops (2PACL). The concept has already proven to be highly reliable and to yield good performance in several HEP experiments [6,7], and even in space applications like the AMS experiment on the International Space Station (ISS) [8].

For designing evaporative cooling systems, knowledge about the appearance and spatial distribution of the co-current vapour and liquid phases is required. Geometric structures of two-phase flows in ducts are

* Corresponding author at: European Organization for Nuclear Research (CERN), CH-1211 Geneva 23, Switzerland.
E-mail address: david.schmid@cern.ch (D. Schmid).
[1] Provided same share of supervision.

https://doi.org/10.1016/j.expthermflusci.2021.110526
Received 20 July 2021; Received in revised form 8 September 2021; Accepted 21 September 2021
Available online 24 October 2021

Nomenclature

Acronyms

2PACL	Two-Phase Accumulator Controlled Loop
AMS	Alpha Magnetic Spectrometer
ATLAS	A Toroidal LHC ApparatuS
ATLAS ITk	ATLAS Inner Tracker
CERN	European Organization for Nuclear Research
CMS	Compact Muon Solenoid
CNN	Convolutional Neural Network
CO_2	Carbon Dioxide
CORA	CO_2 Research Apparatus
DAQ	Data Acquisition
fps	Frames per Second
GWP	Global Warming Potential
HEP	High Energy Physics
HL-LHC	High Luminosity Large Hadron Collider
HVAC	Heating, ventilation, and air conditioning
ISS	International Space Station
LHC	Large Hadron Collider
NIST	National Institute of Standards and Technology
P&ID	Piping and Instrumentation Diagram
PLC	Programmable Logic Controller
RMSE	Root Mean Square Error
RTD	Resistance Temperature Detector
UNICOS	Unified Industrial Control System

Greek Symbols

ϑ	angle of inclination, [°]
μ	Dynamic Viscosity, $[Pa \cdot s = \frac{\mathrm{N\ s}}{\mathrm{m^2}}]$
ρ	Density, $[\frac{\mathrm{kg}}{\mathrm{m^3}}]$
σ	Surface Tension, $[\frac{N}{m}]$

Roman Symbols

d	Diameter, $[m]$
Fr	Froude-Number, [ ]
G	Mass Velocity, $[\frac{\mathrm{kg}}{\mathrm{m^2 s}}]$
g	Gravitational Constant, $g = 9.81$, $[\frac{\mathrm{m}}{\mathrm{s^2}}]$
h	Specific Enthalpy, $[\frac{\mathrm{kJ}}{\mathrm{kg}}]$
j_L	Superficial Liquid Velocity, $j_L = \frac{\dot{V}_L}{A} = \frac{G(1-x)}{\rho_L}$, $[\frac{\mathrm{m}}{\mathrm{s}}]$
j_V	Superficial Vapour Velocity, $j_V = \frac{\dot{V}_V}{A} = \frac{G \cdot x}{\rho_V}$, $[\frac{\mathrm{m}}{\mathrm{s}}]$
$\dot{m}$	Mass Flow Rate, $[\frac{\mathrm{kg}}{\mathrm{s}}]$
p	Pressure, $[bar]$
$\dot{Q}$	Heater Power, $[W]$
Re	Reynolds-Number, [ ]
T	Temperature, [°C]
We	Weber-Number, [ ]
x	Vapour Quality, [ ]

Subscripts

1p	single-phase
2p	two-phase
amb	ambient
bs	bubbly-slug
ca	churn-annular
EH	electrical heater
exp	experimental
in	inlet
l	liquid
lo	liquid only
pred	predicted
r	ratio
sat	saturation
sc	slug-churn
tr	transition
v	vapour
vo	vapour only

characterized by a number of possible interface configurations that can be described and clustered to "patterns" (or "regimes"). Flow pattern maps are useful tools to describe the physical phenomena of two-phase flows and several studies, e.g. Kattan et al. [9,10], Wojtan et al. [11,12], El Hajal et al. [13] and Thome et al. [14], suggest that the flow pattern maps have the potential to enhance accuracy of prediction methods in channels.

1.1. Flow pattern maps for vertical two-phase flow in macroscale tubes

Existing flow pattern maps can be classified according the approaches and strategies followed for their development. Many studies are of experimental nature, where flow pattern data are used to analyse and determine the flow pattern transitions, like the early works by Hewitt and Roberts [15] and Bennett et al. [16], for example. Contrary to this, theoretical approaches derive criteria for concluding on flow pattern transitions by analysing the physical mechanisms that govern the flow pattern transitions. Like this, Taitel et al. [17] elaborated transition models in a theoretical way and verified their theories with experimental data of water–air mixtures in retrospect. In a similar manner, Barnea [18] presented a unified flow pattern map for gas–liquid flows for all kind of pipe inclinations. It combines studies on horizontal and slightly inclined tubes [19–21], studies on vertical upward [17,22,23], vertical downward [24] and on inclined up- and downward flows [25–27].

Rouhani and Sohal [28] conducted a comprehensive literature review with regards to two-phase flow regimes, detection methods, transition criteria, effects of boundaries and external conditions and on existing flow pattern maps. In a similar manner Cheng et al. [29] carried out a comprehensive review focusing on gas-liquid two-phase flow patterns and flow pattern maps at adiabatic and diabatic conditions, including natural working fluids, like ammonia and CO_2. However, vertical two-phase flow of CO_2 has not been treated in both studies.

Many studies, in particular in the 20th century, were initiated by the petrochemical industry and the energy sector, where energy conversion was mainly based on thermodynamic cycles in fossil and nuclear power plants. Hence, most studies at that time were conducted with mixtures of petrochemicals as well as water-steam or, due to simplicity, more often with water–air mixtures. The fluid properties – especially those of petrochemical products – differ significantly from CO_2.

1.2. Flow pattern observations and maps for horizontal two-phase flow of CO_2

Investigations on flow patterns of CO_2 started with the increasing significance of natural refrigerants at the beginning of the 21st century

and were mainly focused on horizontal microchannel-cooling for the HVAC, the power production and the microelectronics industries. The first studies, like the ones from Pettersen [30,31] carried out flow pattern studies in a horizontal glass tube with a bore diameter of 0.98 mm at temperatures of 0°C and 20°C and for mass velocities ranging from 100 to 580 kg m^{-2} s^{-1}. Yun and Kim [32] visualized the flow boiling process of CO_2 in a horizontal rectangular channel (16 x 2 mm) at various test conditions and developed a flow pattern map for horizontal narrow rectangular channels. Schael and Kind [33] presented flow pattern observations and measurements of the heat transfer in a helical grooved micro fin tube and compared those to the results of a smooth tube. They concluded that there is a co-dependence between the transition vapour quality and mass velocity. Gasche [34] conducted studies on CO_2 evaporation inside a horizontal 0.8 mm hydraulic diameter single-microchannel. The flow patterns were visually observed at a saturation temperature of 23.3°C, a heat flux of 1800 W m^{-2}, vapour qualities from 0.005 to 0.88 and mass velocities ranged from 58 to 235 kg m^{-2} s^{-1}. Three flow regimes had been identified within that study: plug flow at low vapour qualities ($x < 0.25$), slug flow ($0.25 < x < 0.5$) and annular flow ($x > 0.5$).

Thome and Ribatski [35] summarized two-phase flow pattern observations of CO_2 available at that time in a "state-of-the-art" review. Within that work, data of some of the previously mentioned studies were compared to the horizontal flow pattern map for CO_2 of Yun and Kim [32] and the universally applicable maps of Thome-El Hajal [36] and Steiner [37]. None of the maps was able to predict the flow pattern transitions of the CO_2 data properly.

Cheng et al. [38,39] published an updated flow pattern map, based on the work of Wojtan et al. [11], for horizontal two-phase flow of CO_2 that is intrinsically related to the corresponding heat transfer mechanisms. Later, this work has been updated by Cheng et al. [40] and a map with an extended range of validity has been presented.

Mastrullo et al. [41] carried out flow visualizations during flow boiling of CO_2 in a horizontal smooth tube of 6 mm inner diameter and identified flow regime transitions from slug-to-intermittent, intermittent-to-annular and at the dryout inception. They varied the mass velocity from 150 to 500 kg m^{-2} s^{-1} and the reduced pressures from 0.57 to 0.64 during their experiments. This corresponds to saturation temperatures of 7.3°C and 12°C and is therefore far from the low temperature operation in HEP detectors.

In their most recent review, Cheng et al. [42] summarized flow pattern visualizations of CO_2 two-phase flow conducted after 2007 and compared them to the generalized flow pattern map [40]. Good agreement between the new flow pattern observations and the generalized flow pattern map has been found. However, vertical flow pattern observations are not mentioned in this study.

1.3. Nature of the issue, objectives and scope of the present work

Literature offers a large number of flow pattern maps for any kind of pipe orientation for liquid–gas mixtures, water and synthetic refrigerants, while several flow regime observations are available for horizontal CO_2 two-phase flow, mainly for microchannel applications. However, there are no flow pattern observations available for vertical two-phase flow of CO_2 and as a consequence, there is no validated flow pattern map available for vertical orientations.

To fill in this void, a comprehensive test program was carried out to (1) develop a database of flow pattern observations for CO_2 two-phase flow in vertical direction and (2) to provide a flow pattern map as a tool for further research on vertical CO_2 two-phase flow.

An experimental setup has been built at CERN that allows flow pattern visualization in both vertical upward and downward direction. Based on these observations, the transitions between flow regimes are investigated and condensed into novel flow pattern maps for vertical upward and downward CO_2 two-phase flows.

2. Experimental methodology and database

2.1. The test facility, uncertainties of instrumentation and data reduction

The test facility built within the scope of the present study consists of two consecutive test sections in order to investigate two-phase flow characteristics in vertical upward and downward direction. The entire setup is made of stainless steel tubes (EN 1.4404) with an inner diameter of 8 mm, which corresponds to the same hydraulic diameter of the concentric transfer lines currently used in the ATLAS and CMS experiments. According to several studies, like Kew and Cornwell [43], Kandlikar [44] and Ong and Thome [45], the tube size investigated in the present study with CO_2 can be clearly assigned to macrochannels. Fig. 1 shows the piping and instrumentation diagram (P&ID) of the test facility. A refrigeration plant, called CORA (CO_2 Research Apparatus) [46], provides subcooled CO_2 at the inlet of the test setup (location 2010 in Fig. 1) and allows to control the flow parameters and the saturation pressure. The enthalpy at location 2014 can be controlled by means of a 3 kW pre-heater located prior to the inlet of the transparent section. In addition, a 3 kW post-heater allows to determine the enthalpy at the outlet of the setup by fully evaporating the remaining two-phase flow to the single-vapour phase. The pressures and fluid temperatures are monitored at several locations of the test setup with absolute pressure transmitters and RTDs (PT100). The sensor tips of the temperature probes are inserted into the pipe and in direct contact with the fluid, such that the flow is perturbed minimally. The installed instrumentation has been calibrated and the uncertainties are summarized in Table 1. The data acquisition of the instrumentation, as well as the controls of the setup are realized with a PLC based DAQ system and are embedded in CERN's UNICOS environment [47]. Finally, the heat input of the two heaters, as well as the insulation of the entire setup have been validated with single-phase energy balance tests, where the heat pickup has been determined. Based on this, heat fluxes from ambient across the insulation have been considered in the post-processing analysis. The enthalpy at any location of the test rig is determined as follows:

$$h_z = h_{1p,2010} + \frac{\left(\dot{Q}_{\mathrm{EH},1} + \dot{Q}_{amb}\right)}{\dot{m}} \tag{1}$$

where $h_{1p,2010}$ denotes the single-phase enthalpy at the inlet of the test rig (at location 2010 in Fig. 1) and $\dot{Q}_{\mathrm{EH},1}$ and $\dot{Q}_{amb}$ are the heater power of the pre-heater and the heat pickup from ambient across the insulation. The vapour quality at any location of the setup is derived from the enthalpy h_z.

$$x_z = \frac{h_z - h_l}{h_v - h_l} \tag{2}$$

The calculations are carried out in MATLAB and all the fluid properties are obtained using REFPROP of NIST [48].

2.2. Transparent section and visualization techniques

The vertical test sections have an elevation of 8 m and each of them is equipped with a transparent section for flow visualization at ground level, i.e. at the inlet to the vertical test section in upward direction and at the outlet of the vertical test section in downward direction. The transparent sections are designed modular, so that their positions can be changed within the setup (see Fig. 2). The main components of the transparent sections are thick-walled glass tubes with the same inner diameter as the stainless steel tubes (8 mm) and an outer diameter of 34 mm to withstand the high pressures of CO_2. For safety reasons, the glass tubes are surrounded by a stainless steel box with flat sight glasses at front- and back side respectively. A digital high-speed camera PHOTRON FASTCAM Mini AX is installed on a mechanical support frame, that can be switched to face any of the transparent sections. High-speed frames and videos were recorded at two different camera

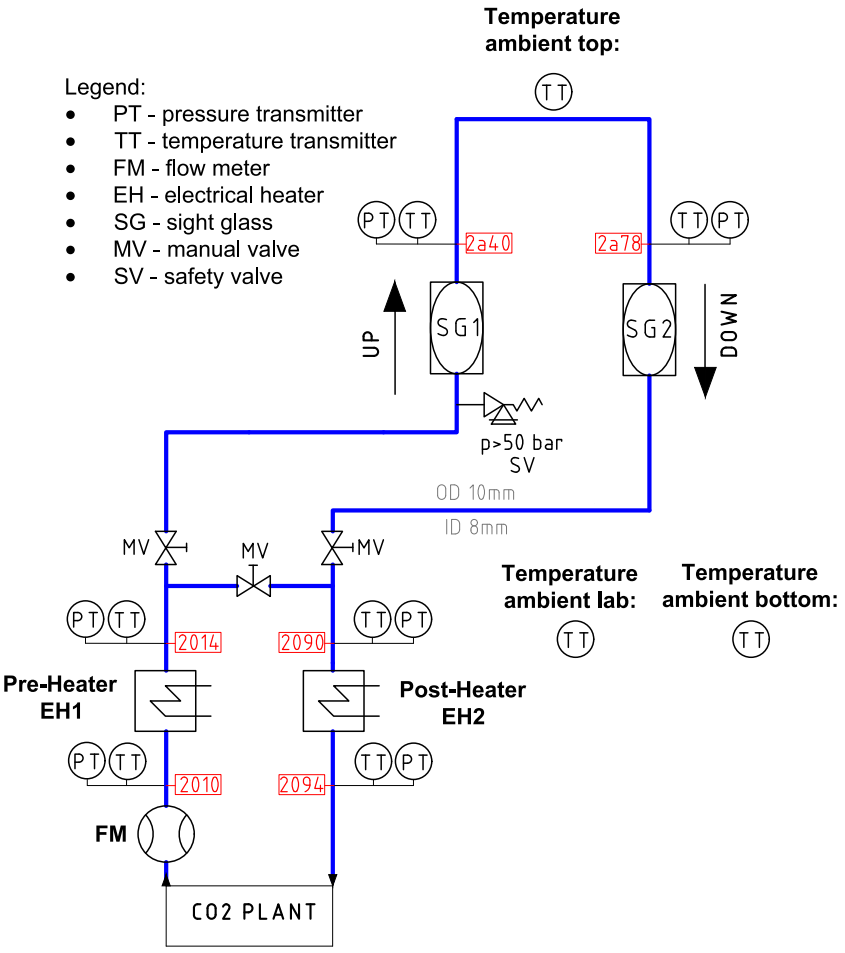

Fig. 1. Simplified piping and instrumentation diagram (P&ID) of the test facility.

Table 1
Uncertainties of the calibrated instrumentation and property calculations.

Parameter	Brand/type	Uncertainty of	
Pressure, p	KELLER PAA-33X	±0.07 %	measurem.
Temperature, T	PT100	±55 mK	measurem.
Mass flow rate, $\dot{m}$	KROHNE Optimass 3300C S03	±0.15 %	measurem.
Mass velocity, G	–	±2.35 %	value
Enthalpy, single-phase, h_{1p}	–	±0.075 %	value
Enthalpy, two-phase, h_{2p}	–	±0.525 %	value
Vapour quality, x	–	±0.3...0.9 %	value

Table 2
Camera settings for the recording of the high-speed images.

Parameter	Settings 1	Settings 2
Resolution	512 x 512	384 x 384
Frame rate	13600 fps	
Shutter speed	1/300000 s	
Period of time recorded	1.61 s	2.86 s
No. of frames recorded	21850	38840
Percentage of data archived	10 %	

settings that are listed in Table 2. The refraction due to the thick-walled glass tubes are taken into account according to the approach by Fu et al. [49]. For calibrating the refraction effect, a calibrated checkerboard pattern was inserted into the glass tubes and images were recorded with the high-speed camera prior to data collection.

2.3. Test conditions and database

The test conditions are specified primarily by the requirements of the new ATLAS ITk and CMS Inner Detector and by both the limitations of the test facility and the refrigeration plant.

- The range of saturation temperatures is limited by the chiller capacity of the refrigeration plant and by the maximum pressure the glass tubes are able to withstand. Thus, the investigated ranges of saturation pressures and temperatures are given as follows:

$$16 \text{ bar} \leq p_{sat} \leq 40 \text{ bar}; \quad -26.5°C \leq T_{sat} \leq +5.3°C$$

- The upper limit of the mass velocity is determined by the maximum pump capacity, while the lower one is given by the flow rate, where subcooled conditions are still possible at the transparent sections. Due to the rather long transfer lines from the plant to the vertical test sections of the test rig and the resulting heat

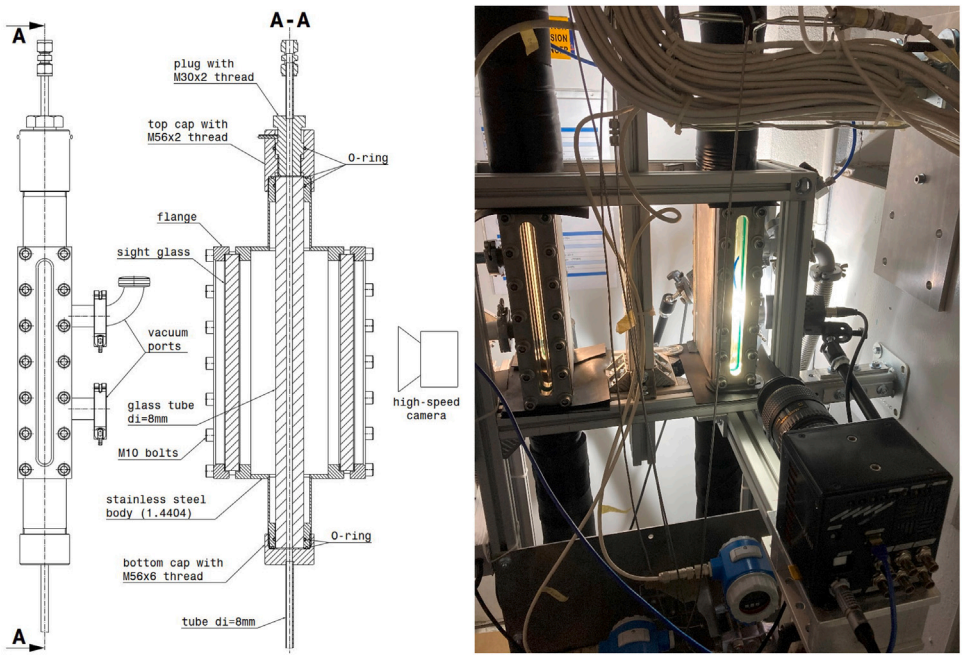

Fig. 2. Transparent section for flow visualization; sectional view (left) and during operation (right).

pickup from ambient, the range of mass velocity also depends on the saturation- and ambient temperatures. This results in a range in the order of

$$100\ \text{kg m}^{-2}\ \text{s}^{-1} \leq G \leq 450\ \text{kg m}^{-2}\ \text{s}^{-1}$$

- The range of vapour quality possible is influenced by the saturation temperature, the mass flow rate and the maximum power of the pre-heater, and therefore varies due to the conditions of the experiment from

$$0 \leq x \leq 1$$

Flow pattern observations in vertical upward and downward direction have been carried out one after another, starting with the vertical upward direction configuration, and then swapping the camera to the transparent section of the vertical downflow and repeating some of the tests. A total of 431 data points have been collected for vertical upflow and 123 data points for the vertical downflow configuration. Fig. 3 gives an overview of the histograms of the test data, that further describe the flow pattern observations used for the flow pattern analysis.

2.4. Flow regime detection methods

Identifying and distinguishing flow patterns properly with the naked eye is challenging in two-phase flows, in particular at flow regime transitions with high vapour qualities, where the flow velocity is increasing. As a consequence, the majority of data reported in the literature has been acquired by taking advantage of high-speed imaging and by identifying the flow pattern transitions by visual evaluation of the records. However, the flow pattern classification based on visual observation remains a subjective appraisal of the observer. In order to obtain unbiased results, Rouhani and Sohal [28] summarized several methods of flow regime classification, like the direct observation methods of high-speed photography, X-ray attenuation, electrical contact probes, or indirect determination methods like static pressure oscillation analysis. At a later point, improved optical measurement and signal processing techniques were implemented for the characterization of flow patterns. Revellin et al. [50] made use of laser- and photodiodes for the characterization of flow patterns in microtubes, whereas Wu and Duan [51] investigated means to classify flow regimes and void fraction measurements by using collimated infrared laser light.

In the present study the recorded high-speed frames and videos are analysed with computer vision and machine learning techniques, making use of Convolutional Neural Networks (CNN). The CNN, based on the ResNet architecture [52], has been trained on a balanced dataset of 39261 input frames that can be clearly assigned to any of the typical two-phase flow classes specified in the next chapter. As a result, a Frame- and Flow-Regime-Classifier has been built, that allows to analyse high-speed videos and outputs the percentage of the video's constituent flow regime classes. The definition of the thresholds, where the transitions are taking place are still the decision of the observer. However, this tool provides objective numbers based on which the decisions can be made. By validating the Frame- and Flow-Regime-Classifier with 26200 "unseen" data points, an accuracy of 95.4 % has been identified.

3. Results and discussion

3.1. Results of flow visualization - Flow pattern observations

The variety of flow pattern classifications appearing in literature is diverse and only few are commonly accepted, like the ones in Fig. 4. The main flow regimes observed in vertical upflow ($\vartheta = +90°$) during operation of this test facility and their transition criteria are described and discussed in the following.

Bubbly flow. The vapour phase is uniformly dispersed in the continuous liquid phase as bubbles that may vary in size and shape. However, they are significantly smaller than the tube diameter and generally tend to be spherical [53]. In the bubbly regime, except for very low mass velocities, where buoyancy effects become noticeable, the ratio of the phase velocities is close to unity and no severe slippage can be observed. This flow pattern develops at vapour qualities around zero and is likely to appear even before the fluid reaches saturated conditions, where subcooled boiling occurs.

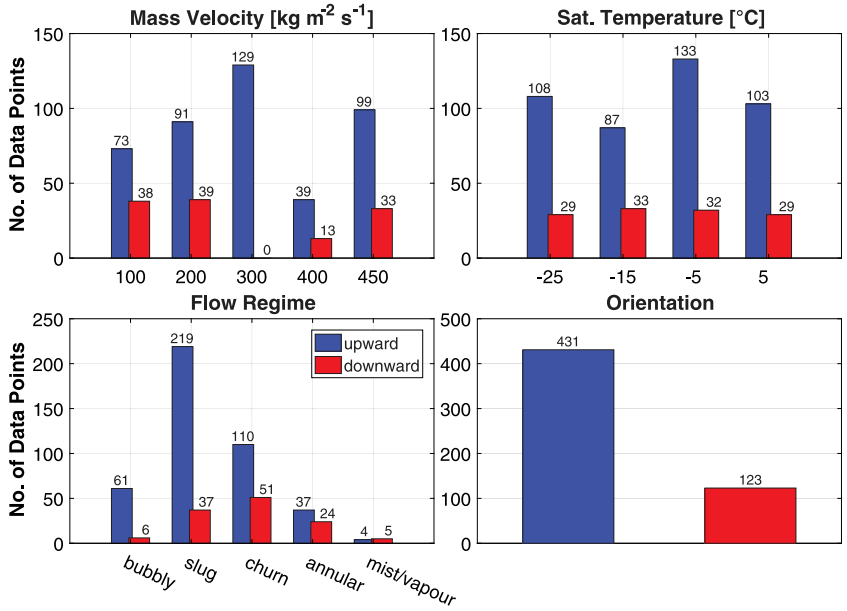

Fig. 3. Histograms describing the experimental database.

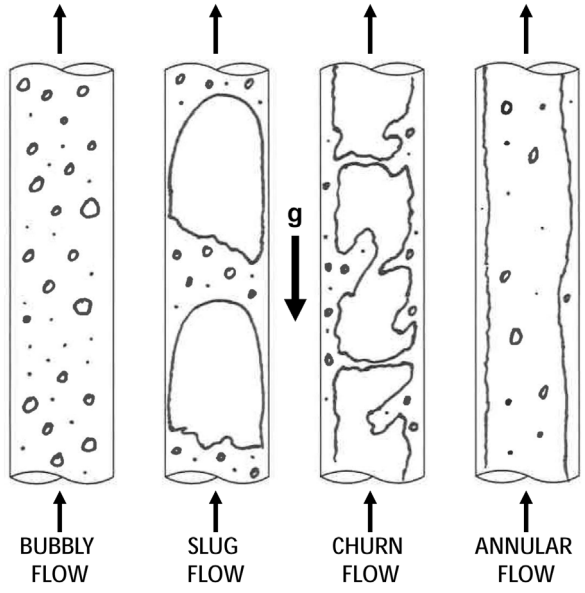

Fig. 4. Typical two-phase flow patterns in vertical upward direction ($\vartheta = +90°$).

Slug flow. With increasing vapour fractions, the bubbles start to coalesce forming larger bubbles nearly in the size of the inner tube diameter. These bubbles typically appear similar to the shape of a bullet with a characteristic hemispherical front and a fluctuating tail in flow direction. They are commonly denoted as "Taylor-Bubbles" [53]. The tube perimeter is typically wetted by a liquid film that – in upward direction – may flow in opposite direction due to gravity [54]. Liquid slugs carrying small bubbles are bridging the pipe perimeters and separate the Taylor-Bubbles from one another. Buoyancy affects the velocity of the phases and in upward direction the net average velocity of the vapour phase is typically higher than the one of the liquid. The Taylor-Bubbles are getting longer as vapour quality increases and as a consequence the liquid slugs appear at lower frequencies.

Churn flow. This flow regime is characterized by a chaotic mix of the phases. It starts developing when the liquid slugs are getting instable and begin to collapse. The local flow direction of the liquid may oscillate between up- and downflow, yet with a net flow in upward direction [53]. In the transition from slug to churn, the vapour concentration (void fraction) in the liquid slugs reaches its maximum and the turbulent wake behind the preceding Taylor-Bubble starts affecting the nose of the following. The transition criteria to churn flow is defined by liquid slugs that are not sustained. Hence, their frequency drops to zero.

Annular flow. Annular flow is characterized by the continuity of the vapour phase in the pipe core with the liquid phase expelled from the centre to the tube perimeter. The main fraction of the liquid phase flows as an annulus – giving the name of the flow regime – at the inner pipe surface and partly as droplets entrained in the vapour core. The velocity of the vapour phase is typically much higher than the one of the liquid annulus. In vertical upflow the liquid film is lifted by the shear forces of the vapour core. However, at low mass velocities, the gravitational forces might exceed the shear and the liquid film flows in opposite direction [55,56]. In the transition from churn to annular flow, the liquid phase is not able to bridge the tube perimeters anymore and the vapour in the pipe core is able to travel freely without being interrupted by the liquid. However, there are no discrete criteria to determine the transition from churn to annular. Hence, it is more a continuous change from a chaotic and turbulent state to a rather steady flow. Furthermore, oscillations between both flow regimes can be observed in the transition phase, where sequences of one regime are followed by sequences of the other. This observation is confirmed by the results of the Frame- and Flow Regime Classifier that does not yield a clear change in flow regime either. Instead, it is more a continuous transition, where the percentage of frames classified as "annular" rises as vapour quality keeps increasing.

Mist and vapour flow. This flow pattern can be seen as the inverse of pure liquid at the onset of bubbly flow where the vapour phase is continuous and liquid is present only as small entrained droplets. The tube surface is in direct contact with the vapour phase and the annular liquid film has dried out, which defines the characteristic transition criteria from annular to mist and vapour flow. In contrast to horizontal flows, the dryout in vertical direction is happening symmetrically and no partial break up of the liquid film due to gravity can be observed. Hence, mist or vapour flow only occurs when the mass fraction of the liquid phase is nearly zero. In turn, the mass fraction of the vapour

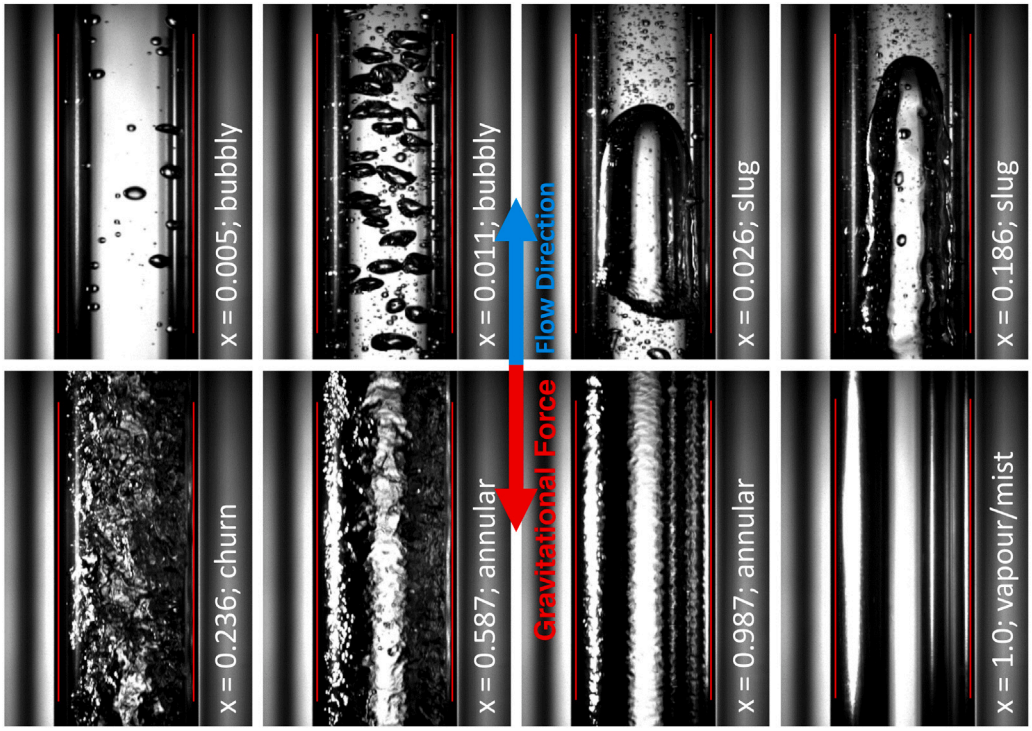

Fig. 5. Flow pattern observations of CO_2 in vertical upward direction ($\vartheta = +90°$) at $T_{sat} = -25°C$; $G = 200$ kg m^{-2} s^{-1}; vapour quality increasing from top left to bottom right: bubbly, bubbly, slug, slug, churn, annular, annular, vapour/mist. The red lines represent the inner tube walls.

phase is close to one and the droplets sometimes persist even beyond that point in the superheated vapour phase.

Fig. 5 shows an example of flow pattern observations of CO_2 in vertical upward direction recorded at the CERN test facility at a saturation temperature of −25°C and a mass velocity of 200 kg m^{-2} s^{-1}. Throughout all experiments, running from low to high vapour qualities, the sequential passing through the previously described flow regimes can be observed.

Flow patterns in vertical downflow ($\vartheta = -90°$) are observed to be similar to those of vertical upflow. However, there are some differences, mainly due to the buoyancy force that is opposed to the flow direction. In bubbly flow, in particular at low mass velocities, the flow directions of the vapour and liquid phases might be counter-current. Tiny bubbles are hardly affected by buoyancy and are therefore travelling downward at a velocity that is in the same order as the liquid phase. With increasing bubble sizes, buoyancy is increasing and the bubbles are slowed down, stagnant or even rising in counter-current direction. However, big Taylor-Bubbles similar in size to the tube diameter are pushed downwards by the inertia of the liquid flow. In slug flow the nose of the Taylor Bubbles might appear flattened and the tail rounded. In some flow conditions it can be observed that the nose as well as the tail are constantly interacting and coalescing with bubbles and hence both do not show well defined boundaries as it is usually the case in upward direction. Besides the different flow direction, annular and mist downflow do not show significant differences to upflow. Fig. 6 shows an example of flow regimes observed in vertical downflow at a saturation temperature of −25°C and a mass velocity of 200 kg m^{-2} s^{-1}.

3.2. Flow pattern observations compared to existing maps and transition lines

A fundamental question in further analysing the flow pattern observations of CO_2 is whether the flow regime transitions can be properly described by generalized flow pattern maps available in literature. Fig. 7 compares all data in upward direction to the work by Barnea [18], that is one of the most widely used flow pattern charts and which has been drawn based on results of air–water mixtures. The transition lines from bubbly to slug (line B) and from churn to annular (J) qualitatively capture the trend of the transitions, however, they significantly offset along the superficial vapour velocity j_v on the abscissa. The transition line from slug to churn flow (H) does not represent the transition of the CO_2 data at all.

Some more studies are compared to CO_2 data in Fig. 8. The bubbly-to-slug transition lines of Taitel et al. [17], Weisman and Kang [57] and Mukherjee and Brill [58] show similar trends to curve B of the Barnea [18] chart in Fig. 7 and are off the CO_2 data. The slug-to-churn transition boundaries from Taitel et al. [17] and McQuillan and Whalley [23,59] are not applicable for CO_2 at all. Only the theoretically derived slug-to-churn transition line from Chen and Brill [60] qualitatively represents the trend, however, not in a satisfactory manner. For the churn-to-annular transition, none of these studies describes the change in flow regime properly. In general, as illustrated in Fig. 8, neither the theoretical studies of Taitel et al. [17] (validated with water–air mixtures), McQuillan and Whalley [23] (air–water, steam–water, R11, R12, R113) and Chen and Brill [60] (air–water), nor the empirical approaches by Weisman and Kang [57] (air–water, air–glycerol, R113) and Mukherjee and Brill [58] (kerosene–air, oil–air) are able to predict the transitions of the present CO_2 data properly.

Many of the previously mentioned studies on flow pattern transitions in vertical direction represent their charts using the superficial phase velocities as coordinates. The superficial phase velocities are defined as the volumetric flow rates of the phases in respect to the cross-sectional area of the channel. In mixtures, the volumetric flow rates of the respective gas and liquid phases are independent and can be measured and varied individually just before blending. Contrary to this, the volumetric flow rates of the phases in saturated single-component flows are co-dependent and the superficial velocities of a boiling fluid are functions of the phase densities. Apart from some exceptions, the vast majority of vertical flow pattern maps mentioned in literature have been validated with flow pattern data of two-component mixtures only. For that reason it is not surprising that none of the known correlations predicts the flow pattern data of pure CO_2 boiling flows properly.

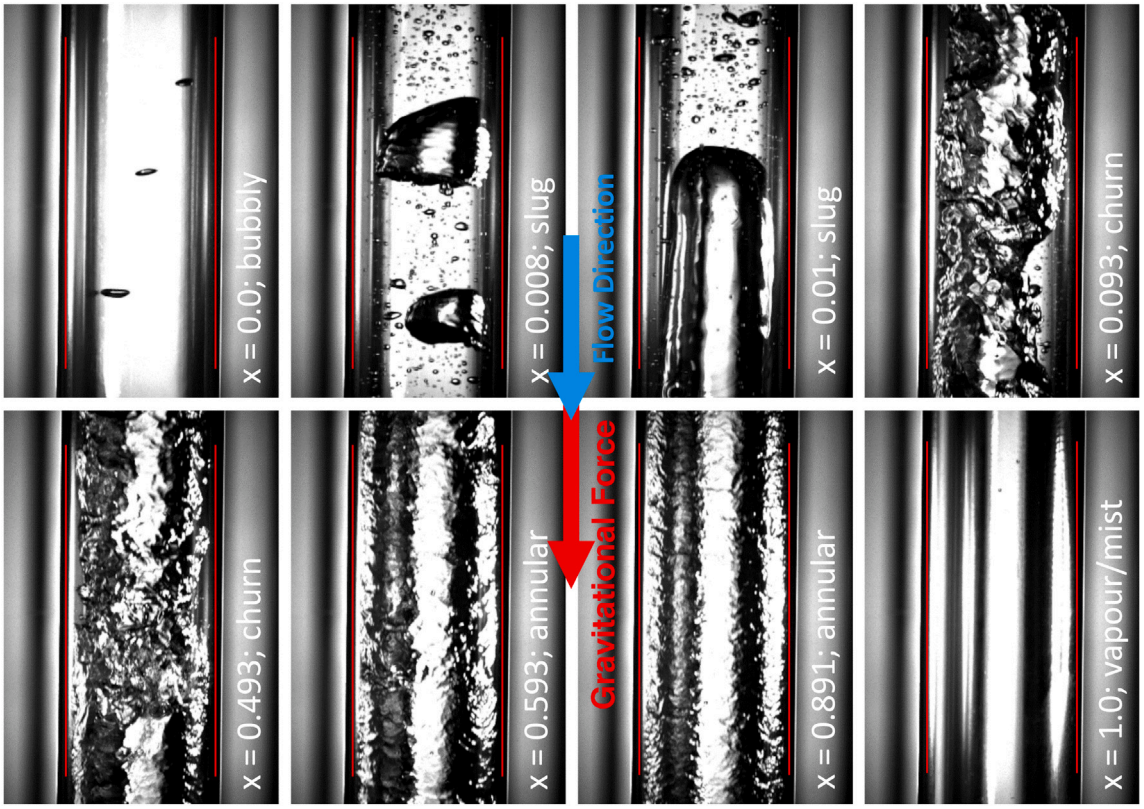

Fig. 6. Flow pattern observations of CO_2 in vertical downward direction ($\vartheta = -90°$) at $T_{sat} = -25°C$; $G = 200$ kg m^{-2} s^{-1}; vapour quality increasing from top left to bottom right: bubbly, slug, slug, churn, churn, annular, annular, vapour/mist. The red lines represent the inner tube walls.

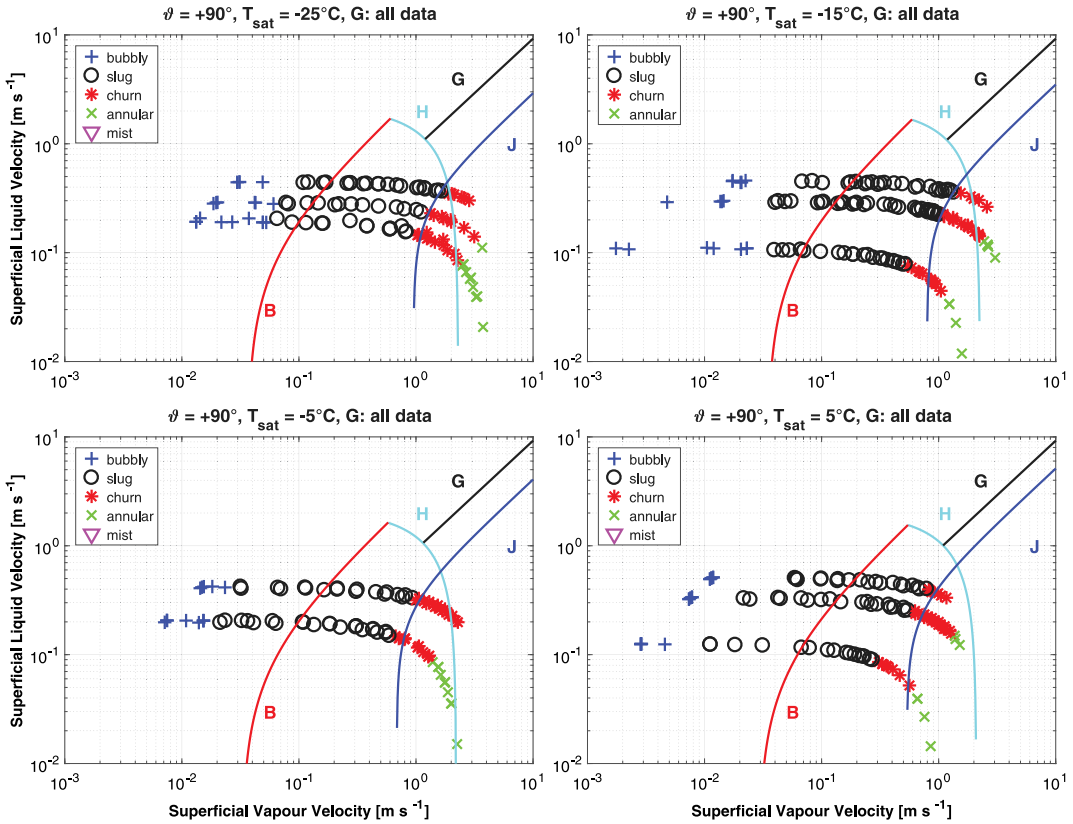

Fig. 7. Flow regime observations of CO_2 two-phase flow in vertical upward direction (markers) compared to the flow pattern map of Barnea [18] (lines). Curve B represents the transition from bubbly to slug, curve H the transition from slug to churn and curve J the transition from churn to annular flow. Line G gives the transition boundary to dispersed bubble flow. The transition lines were plotted based on the experimental conditions and the fluid properties of CO_2.

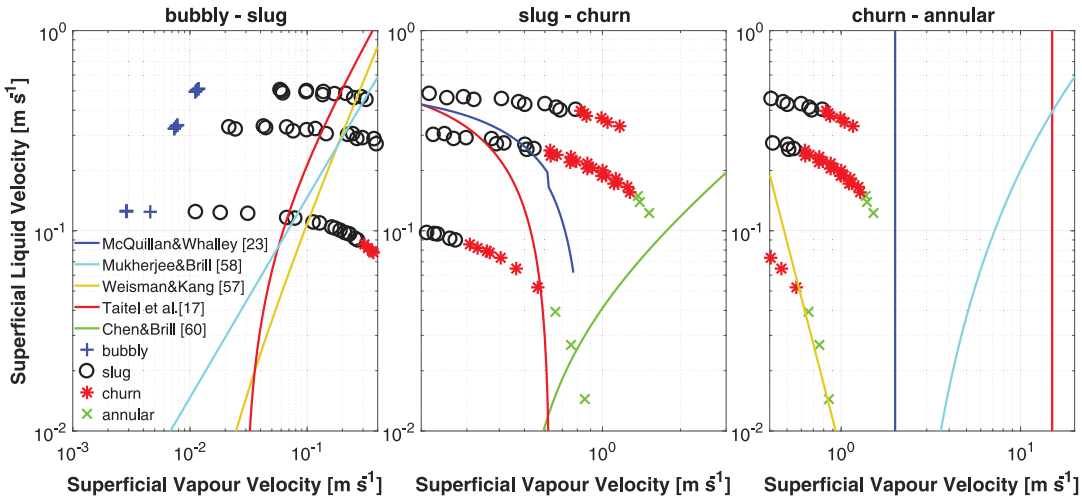

Fig. 8. CO_2 flow pattern observations at T_{sat} = +5°C compared to transition lines of Taitel et al. [17], Weisman and Kang [57], McQuillan and Whalley [23], Mukherjee and Brill [58] and Chen and Brill [60]. The coordinates represent the superficial liquid (j_L) and superficial vapour (j_V) velocities.

An alternative approach for illustrating flow regime transitions are charts using vapour quality and mass velocities as coordinates. Such flow pattern maps can be mainly found in studies of horizontal two-phase flows [11,13,38,40] and are useful in particular for designing evaporators. The abscissa usually represents the vapour quality, therefore the flow patterns at different locations inside an evaporator can be deduced easily from this kind of diagram.

3.3. Development of a new flow pattern map for vertical two-phase flow of CO_2

Flow patterns arise as a consequence of a force balance acting on the co-current phases and are influenced by the fluid properties (saturation temperature/pressure), the flow inertia (mass velocity), vapour quality and the geometry of the duct (angle of inclination, diameter, etc...) [61]. To incorporate the forces acting on the vapour and liquid phases, the transition lines for vertical up- and downflow can be expressed as functions of non-dimensional numbers

$$x_{\mathrm{tr}} = f(G, T_{sat}, d) = f(\mathrm{Re}, \mathrm{We}, \mathrm{Fr}) \tag{3}$$

where x_{tr} represents the vapour quality where the flow regime transition is happening.

The relative influence of inertia and buoyancy are described by the Froude number. In particular at low mass velocities, the inclination of the pipe affects the two-phase flow when the influence of gravitational forces becomes remarkable. This results in low Froude numbers. At high Froude numbers, the inertia is dominant over the gravitational forces and the tube inclination has less influence on the flow patterns [62]. The effects of inertia are incorporated by the Reynolds- and Weber numbers representing the ratios of inertia to viscosity (μ) and surface tension (σ) respectively. The Reynolds number determines whether the flow is laminar or turbulent. Small Reynolds numbers indicate laminar flow, where the inertia forces are irrelevant compared to the viscous forces and disturbances are dissipated [63]. The Weber number provides information about the formation of the liquid/vapour interface. At small Weber numbers the surface tension dominates over inertia what results in smooth interfaces. On the other hand, high Weber numbers indicate high flow inertia and the turbulence perturbs the interface. Furthermore, the density ratio ρ_r is taken into account as well. To simplify the equations, the non-dimensional numbers are considered for all-liquid and all-vapour flow respectively. Eqs. (4)–(10) represent the non-dimensional numbers considered for the development of the transition correlations and Table 3 shows their minimum, maximum and mean values of the experimental domain of this study.

Table 3
Range of non-dimensional numbers of the test campaign.

Non-dim. No.	Min value	Mean value	Max value
Fr_{lo}	0.3386	1.0038	1.7927
Fr_{vo}	3.11	14.38	36.61
Re_{lo}	5289	18900	39640
Re_{vo}	52082	158344	281674
We_{lo}	8.06	120.26	502.85
We_{vo}	176	1567	3931
ρ_r	0.0416	0.0767	0.1279

$$Fr_{lo} = \frac{G}{\rho_l \sqrt{gd}} \tag{4}$$

$$Fr_{vo} = \frac{G}{\rho_v \sqrt{gd}} \tag{5}$$

$$Re_{lo} = \frac{G \cdot d}{\mu_l} \tag{6}$$

$$Re_{vo} = \frac{G \cdot d}{\mu_v} \tag{7}$$

$$We_{lo} = \frac{G^2 \cdot d}{\rho_l \cdot \sigma} \tag{8}$$

$$We_{vo} = \frac{G^2 \cdot d}{\rho_v \cdot \sigma} \tag{9}$$

$$\rho_r = \frac{\rho_v}{\rho_l} \tag{10}$$

The equations describing the flow regime transitions are modelled as a product of non-dimensional numbers, taking the following form:

$$x_{\mathrm{tr}} = a_0 \prod_{i=1}^{N} D_i^{a_i} \tag{11}$$

where D_i represents the non-dimensional number, a_0 is a constant, $a_1 \ldots a_N$ are the corresponding exponents and N corresponds to the amount of non-dimensional numbers used in the respective equation. In order to find the combination and hence the forces that describe the flow regime transition best, all possible combinations of the non-dimensional numbers mentioned in Eqs. (4)–(10) are investigated for each flow regime transition. For $n = 7$, what corresponds to the amount of non-dimensional numbers considered (Eqs. (4)–(10)), this results in 127 possible combinations.

Table 4
Statistics of the identified transition equations.

Transition	Direction	Eq.	Relevant non-dim no.	# Data	RMSE [%]
Bubbly-slug	Up	Eq. (13)	$Fr_{vo}\ Re_{lo}\ We_{vo}$	11	0.1476
	Down	Eq. (14)	$Fr_{vo}\ Re_{lo}\ We_{vo}$	5	0.1827
Slug-churn	Up	Eq. (15)	$Fr_{lo}\ Re_{lo}\ Re_{vo}\ We_{vo}\ \rho_r$	11	0.8155
	Down	Eq. (16)	$Fr_{lo}\ Re_{lo}\ Re_{vo}\ We_{vo}\ \rho_r$	8	1.2329
Churn-annular	Up	Eq. (17)	$Fr_{lo}\ Re_{lo}\ Re_{vo}\ We_{vo}\ \rho_r$	7	1.3916
	Down	Eq. (18)	$Fr_{lo}\ Re_{lo}\ Re_{vo}\ We_{vo}\ \rho_r$	4	$7.5 \cdot 10^{-5}$

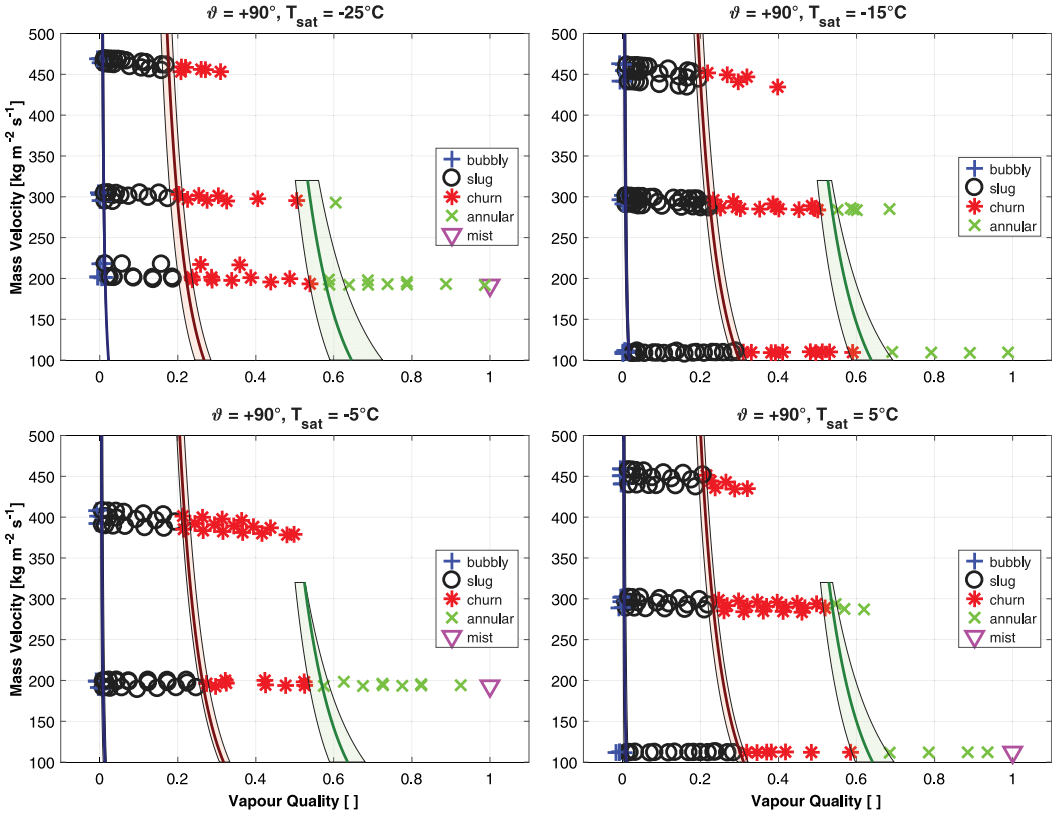

Fig. 9. Identified flow pattern map for vertical upflow of CO_2 in comparison to the test data. The transition zones are determined with data regressions through the first and last data points of the flow regimes.

The constant a_0 and the exponents $a_1 \ldots a_N$ of Eq. (11) are determined with an optimization algorithm, based on an unconstrained multidimensional nonlinear minimization method, carried out in MATLAB. The root mean square error (RMSE) according to

$$RMSE = \sqrt{\frac{1}{k}\sum_{j=1}^{k}\left(x_{j,exp} - x_{j,pred}\right)^2} \tag{12}$$

is chosen as the target value to be minimized, where x_{exp} is the experimental vapour quality at which the change in flow regime is detected, x_{pred} is the predicted transition vapour quality (according to Eq. (11)) and k represents the number of data points available. The experimental transition data x_{exp} is defined as the equidistant value between the extreme data points of two consecutive flow regimes. The final equations for the bubbly-to-slug, slug-to-churn and churn-to-annular flow regime transitions are chosen based on solutions with both low RMSE and low exponents ($a_1 \ldots a_N < |5|$). Eqs. (13)–(18) represent the transition lines for the three flow regime transitions and Table 4 provides their statistics.

The bubbly-to-slug transition in both vertical upward and downward directions is well described by the combination of the all-vapour Froude, the all-liquid Reynolds and the all-vapour Weber number. The combination of the all-liquid Froude number, the all-liquid and all-vapour Reynolds numbers, the all-vapour Weber number and the density ratio gives best results for the slug-to-churn transition for both vertical up- and downflow. Furthermore, the data fit reveals that the set of non-dimensional numbers used to describe the slug-to-churn transition is also an excellent candidate for the churn-to-annular transition providing the lowest RMSE in both up- and downward direction. It can be noticed that each flow regime transition is well described by the same set of non-dimensional numbers for both vertical upflow and downflow respectively.

Bubbly-to-slug transition in vertical upward direction:

$$x_{bs,up} = 17.614 \cdot Fr_{vo}^{0.423} \cdot Re_{lo}^{-0.772} \cdot We_{vo}^{-0.176} \tag{13}$$

Bubbly-to-slug transition in vertical downward direction:

$$x_{bs,\ \mathrm{down}} = 1.3 \cdot 10^{-7} \cdot Fr_{vo}^{1.933} \cdot Re_{lo}^{0.102} \cdot We_{vo}^{0.227} \tag{14}$$

Slug-to-churn transition in vertical upward direction:

$$x_{sc,up} = 2.225 \cdot Fr_{lo}^{0.973} \cdot Re_{lo}^{-1.266} \cdot Re_{vo}^{1.463} \cdot We_{vo}^{-0.721} \cdot \rho_r^{0.809} \tag{15}$$

Slug-to-churn transition in vertical downward direction:

$$x_{sc,down} = 2.604 \cdot Fr_{lo}^{1.068} \cdot Re_{lo}^{-2.299} \cdot Re_{vo}^{1.435} \cdot We_{vo}^{0.588} \cdot \rho_r^{0.923} \tag{16}$$

Churn-to-Annular transition in vertical upward direction:

$$x_{ca,up} = 2.445 \cdot Fr_{lo}^{-0.342} \cdot Re_{lo}^{-0.836} \cdot Re_{vo}^{0.525} \cdot We_{vo}^{0.244} \cdot \rho_r^{0.509} \tag{17}$$

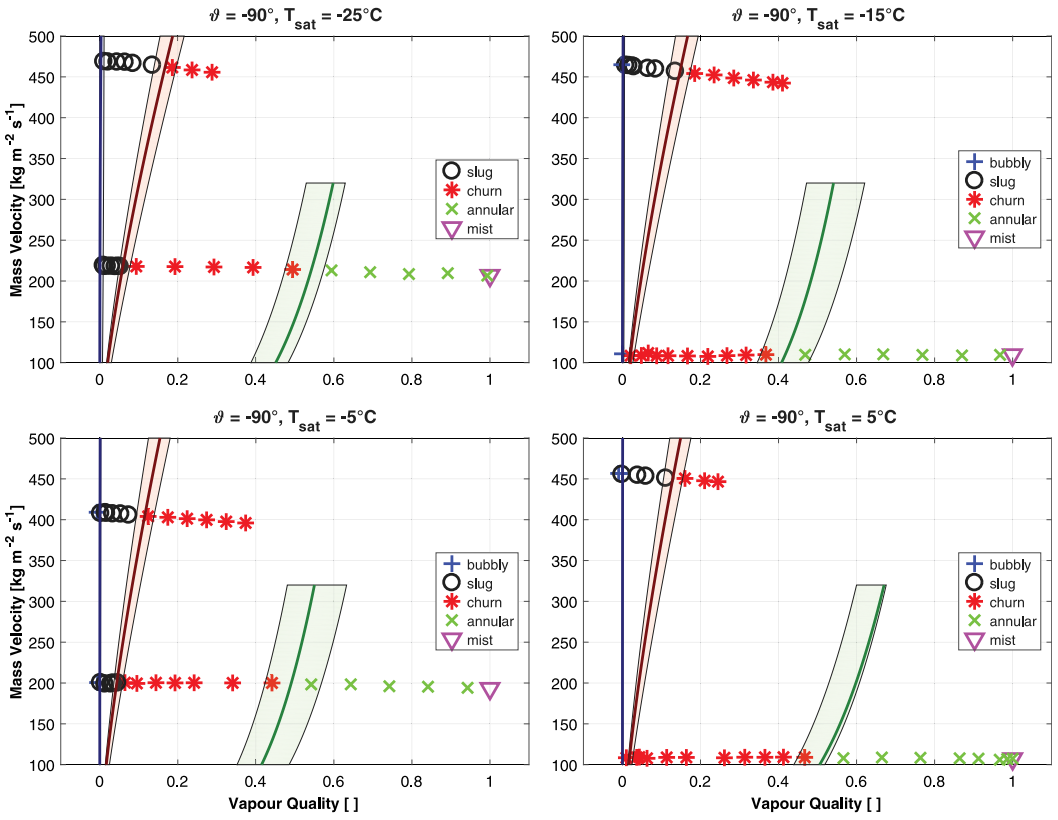

Fig. 10. Identified flow pattern map for vertical downflow of CO_2 in comparison to the test data. The transition zones are determined with data regressions through the first and last data points of the flow regimes.

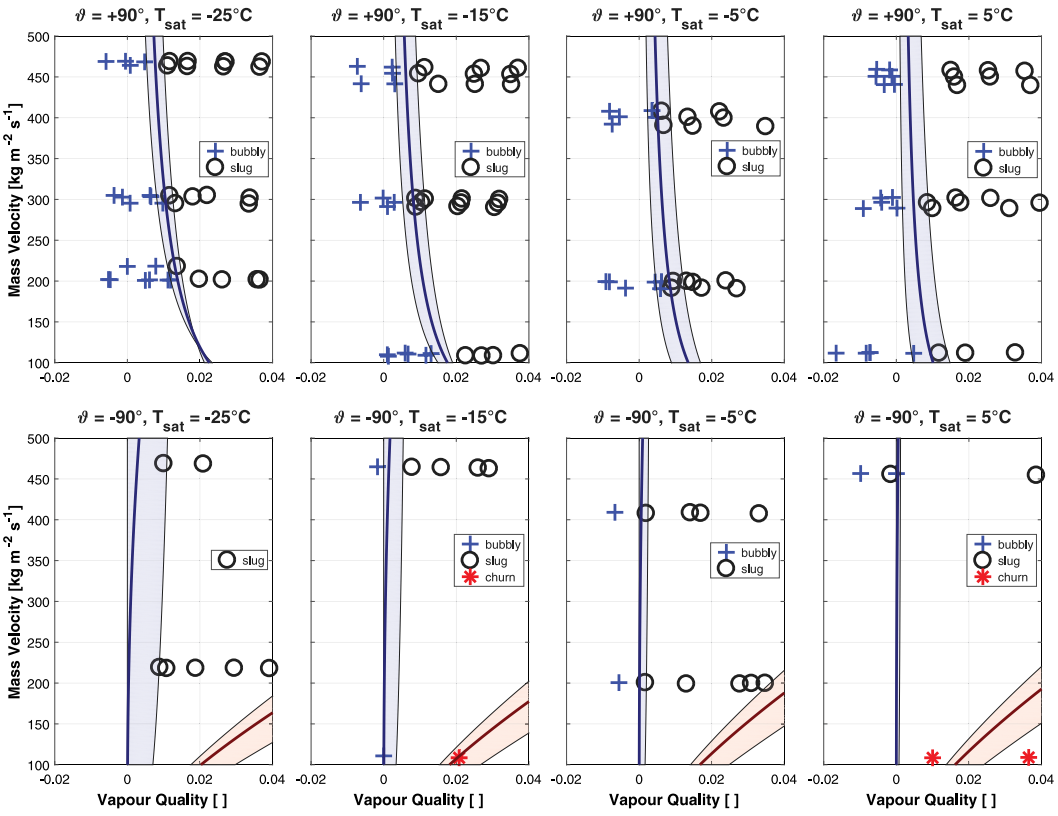

Fig. 11. Detailed view of the bubbly-to-slug flow regime transition in both upward ($\vartheta = +90°$) and downward ($\vartheta = -90°$) direction: transition lines with temperature dependent transition zones.

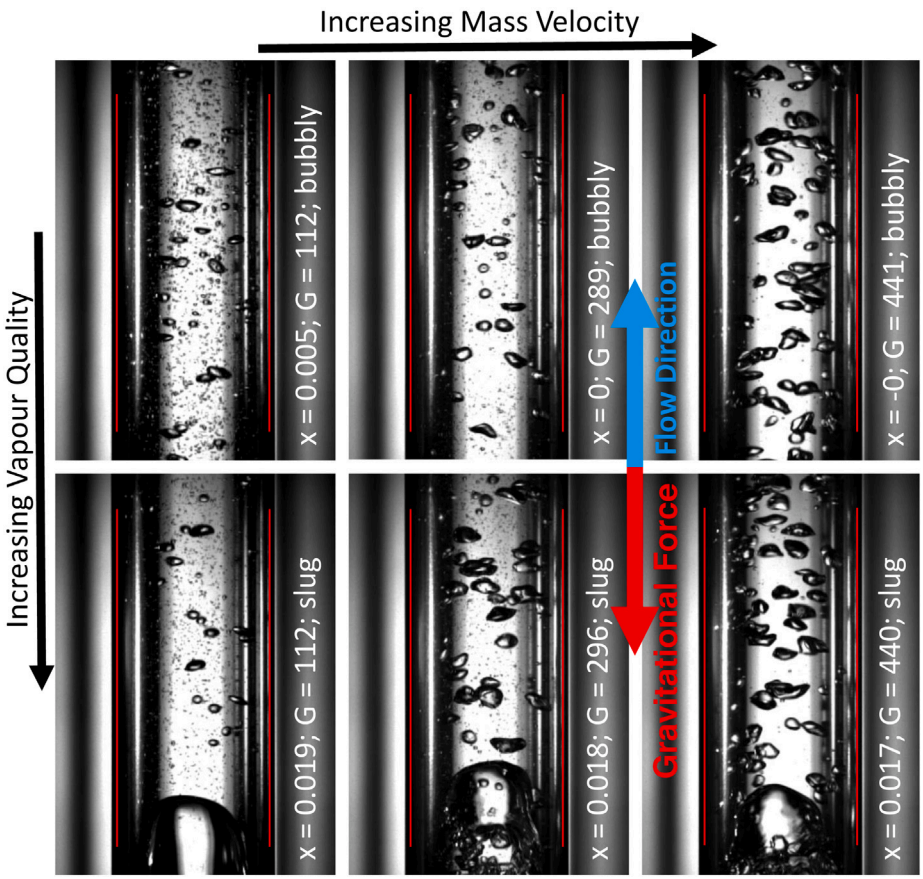

Fig. 12. Influence of mass velocity illustrated with observations of bubbly flow (top row) and slug flow (bottom row) of CO_2 in vertical upward direction ($\vartheta = +90°$) at $T_{sat} = +5°C$. Mass velocity increases from left to right, while vapour quality stays (almost) constant. Finely dispersed bubbles that move upward on a vertical trajectory can be observed at low flow rates. At increased mass velocities, the flow gets turbulent and an increasing coalescence of the bubbles can be noticed.

Churn-to-Annular transition in vertical downward direction:

$$x_{ca,down} = 4.108 \cdot Fr_{lo}^{-2.902} \cdot Re_{lo}^{-4.077} \cdot Re_{vo}^{2.296} \cdot We_{vo}^{2.463} \cdot \rho_r^{2.745} \quad (18)$$

The transition lines and the entire database of flow pattern observations recorded within this study are illustrated in Figs. 9 and 10 for the entire temperature range of the experimental domain ($-25°C \leq T_{sat} \leq +5°C$). Fig. 11 shows detailed views to the bubbly-to-slug transition. In general, it seems more appropriate to identify transition zones instead of transition lines. The changes from one flow regime to another do usually not happen abruptly, it is rather a continuous phenomenon, in particular at the transition from churn to annular, where the transition criteria are rather vaguely defined. The transition zones illustrated in Figs. 9 and 10 are determined with data regressions through the first and last data points of the flow regimes by using the basic structures of non-dimensional numbers according to Eqs. (13)–(18).

In both vertical up- and downward direction the flow regime transitions show a strong correlation between mass velocity and vapour quality. In upward direction, all three flow regime transitions investigated in this study (bubbly-to-slug, slug-to-churn, churn-to-annular) are occurring at increasing vapour qualities when the mass velocity is decreasing. This effect is well incorporated in the upflow transition equations (Eqs. (13), (15), (17)) by an aggregate exponent of mass velocity smaller than zero. In general, this trend is in agreement with the shape of the transition lines presented by Bennett et al. [16] that are based on steam-water observations in vertical upward direction. The data of vertical downflow suggests an inverse behaviour compared to the upflow data, i.e. the transition vapour qualities increase with increasing mass velocity. This corroborates with an overall exponent of mass velocity > 0 in the transition equations for downflow (Eqs. (14), (16), (18)).

The influence of mass velocity in vertical upflow is illustrated in Fig. 12 with frames of bubbly and slug flow, that show an increase in mass velocity, while the vapour quality stays (almost) constant. At low mass velocities, it can be noticed that the flow consists of finely dispersed bubbles varying in size and rising upward on a vertical trajectory, mainly due to buoyancy. On the other hand, the flow is getting more turbulent as mass velocity increases. As a consequence, the bubbles are whirled around inside the tube and an increasing coalescence of the bubbles can be noticed due to the zigzag motion in upward direction. This results in increasing bubble sizes and small bubbles tend to disappear. Hence, in vertical upward direction, bubbly flow persists up to higher vapour qualities at low flow rates, where the flow becomes less turbulent or even laminar and the motion of the bubbles is mainly dominated by the buoyancy forces only.

In downward direction, the regimes of bubbly and slug flow tend to disappear at low mass velocities and the flow immediately turns into churn or annular flow, what is illustrated in Fig. 13. In this case – like in upflow – the inertia of the liquid is becoming negligible and the buoyancy effects are again getting dominant as flow rates are decreasing. As a consequence, phase separation due to buoyancy is happening at low flow rates and the hydrostatic liquid column tends to disappear in the downflow channel. In general, it is observed that the flow regime transitions in upward and downward direction show mirrored trends what can be corroborated by the change from co- to counter-current buoyancy forces.

Moreover, it can be noticed that the bubbly-to-slug and the slug-to-churn transition in upflow show a trend in regard of saturation temperature. According to Fig. 11, the bubbly-to-slug transition in upward direction is happening at higher vapour qualities when decreasing the temperature. This is well captured by Eq. (13), since

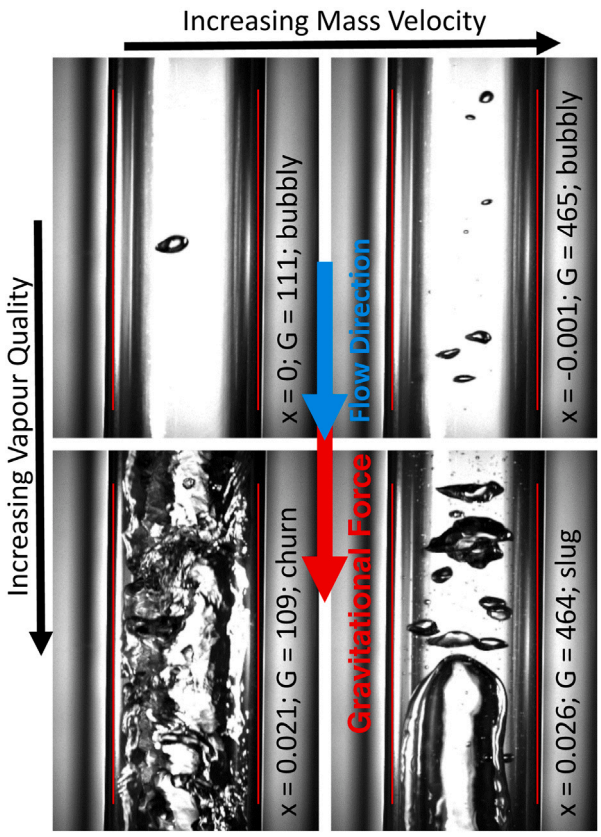

Fig. 13. Influence of mass velocity illustrated with observations of CO_2 in vertical downward direction ($\vartheta = -90°$) at $T_{sat} = -15°C$. Mass velocity increases from left to right, while vapour quality stays (almost) constant. Bubbly flow (top row) immediately turns into churn flow at low mass velocities (bottom left), whereas bubbly flow converts to slug flow at increased flow rates (bottom right).

the vapour density is decreasing and both liquid viscosity and surface tension are increasing at low temperatures. Contrary to this, no bubbly flow can be observed at low temperatures in downward direction, which corroborates observations made in [64]. According to Fig. 9, the slug-to-churn transition vapour quality increases with increasing saturation temperature. This might be linked to the decreasing liquid viscosity that allows slug formation even at higher vapour qualities. It is recommended to consolidate this hypothesis with additional studies over a bigger range of viscosities, e.g. by means of an increased range of saturation temperature or different working fluids. All the other transition lines do not show a clear correlation with temperature, what might be due to the limited amount of data points available.

4. Conclusion

Two-phase flow patterns of vertical up- and downflow of CO_2 are visualized in a dedicated test facility and flow patterns are recorded with a high-speed camera. A database of 431 flow pattern observations in upward and 123 in downward direction is set up and the records are analysed with machine learning techniques, that automatically identify the flow pattern transitions. It is observed that none of the existing flow pattern maps for vertical directions in the literature is able to describe the flow pattern transitions observed within the present study properly. In general it is questionable whether flow pattern maps elaborated with the data of mixtures are able to properly predict the flow pattern transitions of saturated single-component fluids. For that reason, the results of the present study are condensed into novel flow pattern maps for vertical up- and downflow of CO_2 two-phase flow. It is observed, that the changes in flow regime are strongly dependent on vapour quality, mass velocity, the flow direction and the fluid properties. The transition lines in upward and downward direction show opposed trends. This can be mainly substantiated with the changes from co- to counter-current buoyancy forces.

This work provides a baseline for further investigations on the modelling of two-phase flows of CO_2 in vertical direction and expands the existing flow pattern prediction methods for horizontal two-phase flow of CO_2 [40,42] to vertical upward and downward directions. For both vertical channel orientations, the flow patterns of bubbly, slug, annular and mist/vapour flow can be observed. However, some differences to horizontal configurations from literature have been noticed (Fig. 14). In vertical directions, flow stratification, where the co-current phases are clearly separated due to the influence of gravity, is not happening. For the same reason, a dryout region where the liquid film partly disappears, does not occur and the liquid film at the tube walls is drying out symmetrically at vapour qualities just below $x = 1$. Entrained droplets can persist beyond that in the superheated vapour phase.

The lack of other comparable data of vertical two-phase flow of CO_2 in literature can be a motivation for further experimental studies to verify the presented flow pattern maps. Furthermore, there is the potential to extend the range of validity by investigating beyond the test conditions of the present work in terms of mass velocity, saturation temperature, channel size and shape, as well as inclination angle. For the thermal management of future High Energy Physics experiments it is of particular interest to explore the two-phase flow behaviour of CO_2 at temperatures below −30°C, as well as investigating different channel sizes and geometries. Concentric, vertical transfer lines require further studies in concentric annuli and for the design of vertical evaporators, it would be beneficial to analyse the differences to mini- and micro-channels, where capillary forces are becoming significant. It is also recommended to extend the ranges of viscosities and densities in future studies to intensify the examination of the dependency of flow pattern transitions on these fluid properties.

CRediT authorship contribution statement

David Schmid: Conceptualization, Methodology, Software, Validation, Formal analysis, Investigation, Resources, Data curation, Writing – original draft, Writing – review & editing, Visualization, Project administration. **Bart Verlaat:** Conceptualization, Methodology, Validation, Resources, Writing – review & editing, Supervision. **Paolo Petagna:** Conceptualization, Validation, Resources, Writing - review & editing, Funding acquisition. **Rémi Revellin:** Conceptualization, Methodology, Validation, Resources, Writing – review & editing, Supervision. **Jürg Schiffmann:** Conceptualization, Methodology, Validation, Resources, Writing – review & editing, Supervision.

Declaration of competing interest

The authors declare that they have no known competing financial interests or personal relationships that could have appeared to influence the work reported in this paper.

Acknowledgments

These investigations are supported by the European Organization for Nuclear Research (CERN) and the ATLAS experiment. The authors express their thanks to the University of Cape Town (UCT), in particular to Shai Dakota KADISH and his supervisors Prof. Edward BOJE and Mr. Jarryd SON, for developing a CNN-based Frame- and Flow Regime Classifier.

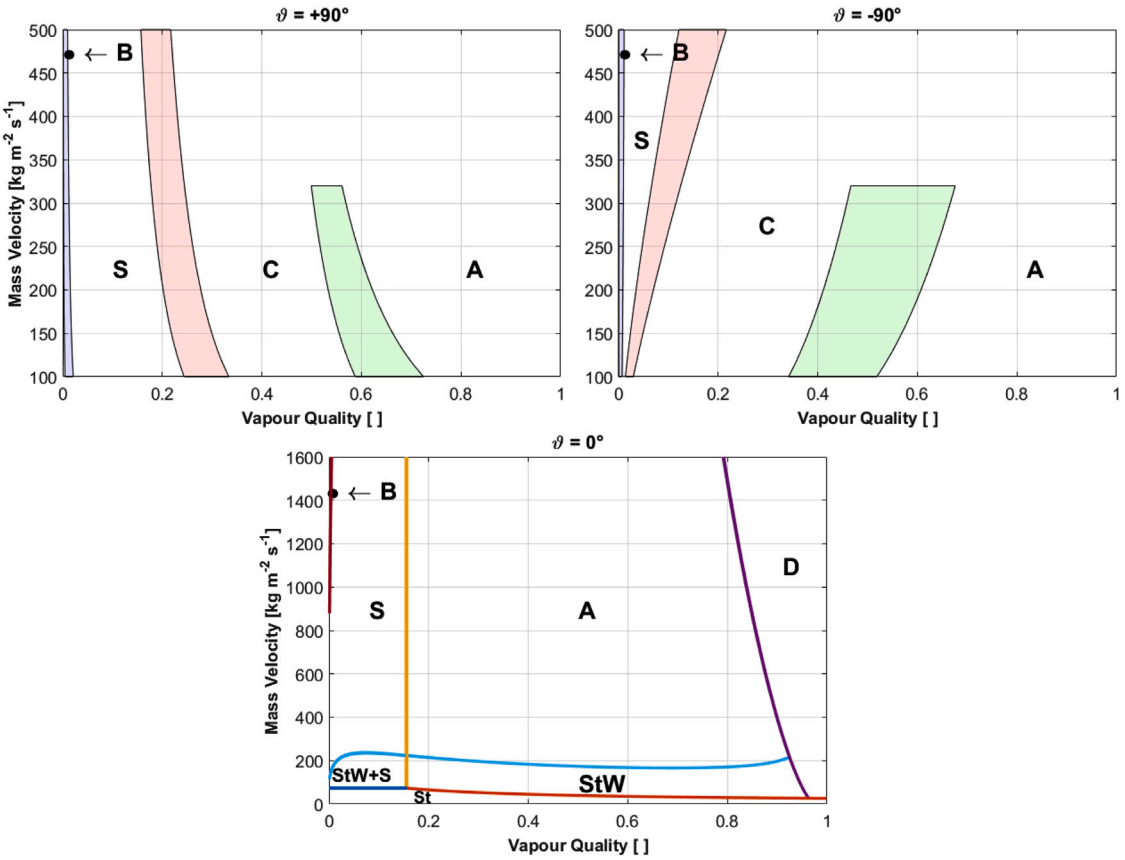

Fig. 14. Flow pattern maps for vertical upward (top left) and downward (top right) direction of CO_2 elaborated within this study in combination with the horizontal flow pattern map of Cheng et al. [40] (bottom). The novel transition zones in the vertical up- and downflow maps are applicable for saturation temperatures $-25°C \leq T_{sat} \leq +5°C$. B: bubbly, S: slug, C: churn, A: annular, D: dryout, St: stratified, StW: stratified-wavy.

References

[1] B. Verlaat, M. Ostrega, L. Zwalinski, C. Bortolin, S. Vogt, J. Godlewski, O. Crespo-Lopez, M.V. Overbeek, T. Blaszcyk, The ATLAS IBL CO_2 cooling system, J. Instrum. 12 (02) (2017) C02064, http://dx.doi.org/10.1088/1748-0221/12/02/C02064, URL https://iopscience.iop.org/article/10.1088/1748-0221/12/02/C02064.

[2] L. Feld, W. Karpinski, J. Merz, M. Wlochal, CO_2 cooling for the CMS tracker at SLHC, J. Instrum. 6 (01) (2011) C01091, http://dx.doi.org/10.1088/1748-0221/6/01/C01091, URL https://iopscience.iop.org/article/10.1088/1748-0221/6/01/C01091.

[3] Verlaat, M. Van Beuzekom, A. Van Lysebetten, CO_2 cooling for HEP experiments, in: Proceedings of the Topical Workshop on Electronics for Particle Physics, TWEPP-2008, CERN, Naxos, Greece, 2008, pp. 328–336, http://dx.doi.org/10.5170/CERN-2008-008.328, URL http://cds.cern.ch/record/1158652.

[4] B. Verlaat, A. Colijn, H. Postema, The future of CO_2 cooling in particle physics detectors, in: International Conference of Refrigeration, ICR11-B2-309, Prague, Czech Republic, 2011, p. 8.

[5] P. Tropea, J. Daguin, D. Giakoumi, N. Koss, P. Petagna, H. Postema, D. Schmid, B. Verlaat, L. Zwalinski, Advancements and plans for the LHC upgrade detector thermal management with CO_2 evaporative cooling, Nucl. Instrum. Methods Phys. Res. A 936 (2019) 644–645, http://dx.doi.org/10.1016/j.nima.2018.10.083, URL https://linkinghub.elsevier.com/retrieve/pii/S0168900218313974.

[6] B. Verlaat, Controlling a 2-phase CO_2 loop using a 2-phase accumulator, in: International Conference of Refrigeration, ICR07-B2-1565, Beijing, China, 2007.

[7] P. Petagna, B. Verlaat, A. Francescon, Two-phase thermal management of silicon detectors for high energy physics, in: J.R. Thome (Ed.), Encyclopedia of Two-Phase Heat Transfer and Flow III: Macro and Micro Flow Boiling and Numerical Modeling Fundamentals Volume 4: Special Boiling Topics, Vol. 4, World Scientific, 2018, pp. 335–412, http://dx.doi.org/10.1142/10656-vol4, URL https://www.worldscientific.com/worldscibooks/10.1142/10656-vol4.

[8] B. Verlaat, H.B. Rookhuizen, A.A.M. Delil, A. Woering, E. Perrin, M. Pohl, R. Battiston, Feasibility demonstration of a mechanically pumped two-phase CO_2 cooling loop for the AMS-2 tracker experiment, in: AIP Conference Proceedings, Vol. 4, AIP, Albuquerque, New Mexico (USA), 2002, pp. 57–64, http://dx.doi.org/10.1063/1.1449708, URL http://aip.scitation.org/doi/abs/10.1063/1.1449708.

[9] N. Kattan, J.R. Thome, D. Favrat, Flow boiling in horizontal tubes: Part 1 – Development of a diabatic two-phase flow pattern map, J. Heat Transfer 120 (1) (1998) 140–147, http://dx.doi.org/10.1115/1.2830037, URL https://asmedigitalcollection.asme.org/heattransfer/article/120/1/140/383031/Flow-Boiling-in-Horizontal-Tubes-Part-1Development.

[10] N. Kattan, J.R. Thome, D. Favrat, Flow boiling in horizontal tubes: Part 3 – Development of a new heat transfer model based on flow pattern, J. Heat Transfer 120 (1) (1998) 156–165, http://dx.doi.org/10.1115/1.2830039, URL https://asmedigitalcollection.asme.org/heattransfer/article/120/1/156/383006/Flow-Boiling-in-Horizontal-Tubes-Part-3Development.

[11] L. Wojtan, T. Ursenbacher, J.R. Thome, Investigation of flow boiling in horizontal tubes: Part I – A new diabatic two-phase flow pattern map, Int. J. Heat Mass Transfer 48 (14) (2005) 2955–2969, http://dx.doi.org/10.1016/j.ijheatmasstransfer.2004.12.012, URL https://linkinghub.elsevier.com/retrieve/pii/S0017931005000268.

[12] L. Wojtan, T. Ursenbacher, J.R. Thome, Investigation of flow boiling in horizontal tubes: Part II – Development of a new heat transfer model for stratified-wavy, dryout and mist flow regimes, Int. J. Heat Mass Transfer 48 (14) (2005) 2970–2985, http://dx.doi.org/10.1016/j.ijheatmasstransfer.2004.12.013, URL https://linkinghub.elsevier.com/retrieve/pii/S001793100500027X.

[13] J. El Hajal, J. Thome, A. Cavallini, Condensation in horizontal tubes, part 1: two-phase flow pattern map, Int. J. Heat Mass Transfer 46 (18) (2003) 3349–3363, http://dx.doi.org/10.1016/S0017-9310(03)00139-X, URL https://linkinghub.elsevier.com/retrieve/pii/S001793100300139X.

[14] J. Thome, J. El Hajal, A. Cavallini, Condensation in horizontal tubes, part 2: New heat transfer model based on flow regimes, Int. J. Heat Mass Transfer 46 (18) (2003) 3365–3387, http://dx.doi.org/10.1016/S0017-9310(03)00140-6, URL https://linkinghub.elsevier.com/retrieve/pii/S0017931003001406.

[15] G.F. Hewitt, D.N. Roberts, Studies of two-phase flow patterns by simultaneous x-ray and flash photography, 1969, https://www.osti.gov/biblio/4798091.

[16] B.A.W. Bennett, G.F. Hewitt, H.A. Kearsey, R.K.F. Keeys, P.M.C. Lacey, Flow visualization studies of boiling at high pressure, Proc. Inst. Mech. Eng. Conf. Proc. 180 (3) (1965) 260–283, http://dx.doi.org/10.1243/PIME_CONF_1965_180_119_02, URL http://journals.sagepub.com/doi/10.1243/PIME_CONF_1965_180_119_02.

[17] Y. Taitel, D. Bornea, A.E. Dukler, Modelling flow pattern transitions for steady upward gas-liquid flow in vertical tubes, AIChE J. 26 (3) (1980) 345–354,

http://dx.doi.org/10.1002/aic.690260304, URL http://doi.wiley.com/10.1002/aic.690260304.

[18] D. Barnea, A unified model for predicting flow-pattern transitions for the whole range of pipe inclinations, Int. J. Multiph. Flow. 13 (1) (1987) 1–12, http://dx.doi.org/10.1016/0301-9322(87)90002-4, URL https://linkinghub.elsevier.com/retrieve/pii/0301932287900024.

[19] Y. Taitel, A.E. Dukler, A model for predicting flow regime transitions in horizontal and near horizontal gas-liquid flow, AIChE J. 22 (1) (1976) 47–55, http://dx.doi.org/10.1002/aic.690220105, URL http://doi.wiley.com/10.1002/aic.690220105.

[20] V. Kadambi, Stability of annular flow in horizontal tubes, Int. J. Multiph. Flow. 8 (4) (1982) 311–328, http://dx.doi.org/10.1016/0301-9322(82)90045-3, URL https://linkinghub.elsevier.com/retrieve/pii/0301932282900453.

[21] P.Y. Lin, T.J. Hanratty, Prediction of the initiation of slugs with linear stability theory, Int. J. Multiph. Flow. 12 (1) (1986) 79–98, http://dx.doi.org/10.1016/0301-9322(86)90005-4, URL https://linkinghub.elsevier.com/retrieve/pii/0301932286900054.

[22] M. Kaichiro, M. Ishii, Flow regime transition criteria for upward two-phase flow in vertical tubes, Int. J. Heat Mass Transfer 27 (5) (1984) 723–737, http://dx.doi.org/10.1016/0017-9310(84)90142-X, URL https://linkinghub.elsevier.com/retrieve/pii/001793108490142X.

[23] K.W. McQuillan, P.B. Whalley, Flow patterns in vertical two-phase flow, Int. J. Multiph. Flow. 11 (2) (1985) 161–175, http://dx.doi.org/10.1016/0301-9322(85)90043-6, URL https://linkinghub.elsevier.com/retrieve/pii/0301932285900436.

[24] D. Barnea, O. Shoham, Y. Taitel, Flow pattern transition for vertical downward two phase flow, Chem. Eng. Sci. 37 (5) (1982) 741–744, http://dx.doi.org/10.1016/0009-2509(82)85034-3, URL https://linkinghub.elsevier.com/retrieve/pii/0009250982850343.

[25] D. Barnea, N. Brauner, Holdup of the liquid slug in two phase intermittent flow, Int. J. Multiph. Flow. 11 (1) (1985) 43–49, http://dx.doi.org/10.1016/0301-9322(85)90004-7, URL https://linkinghub.elsevier.com/retrieve/pii/0301932285900047.

[26] D. Barnea, O. Shoham, Y. Taitel, Flow pattern transition for downward inclined two phase flow; horizontal to vertical, Chem. Eng. Sci. 37 (5) (1982) 735–740, http://dx.doi.org/10.1016/0009-2509(82)85033-1, URL https://linkinghub.elsevier.com/retrieve/pii/0009250982850331.

[27] D. Barnea, Transition from annular flow and from dispersed bubble flow – unified models for the whole range of pipe inclinations, Int. J. Multiph. Flow. 12 (5) (1986) 733–744, http://dx.doi.org/10.1016/0301-9322(86)90048-0, URL https://linkinghub.elsevier.com/retrieve/pii/0301932286900480.

[28] S.Z. Rouhani, M.S. Sohal, Two-phase flow patterns: A review of research results, Prog. Nucl. Energy 11 (3) (1983) 219–259, http://dx.doi.org/10.1016/0149-1970(83)90012-4, URL https://linkinghub.elsevier.com/retrieve/pii/0149197083900124.

[29] L. Cheng, G. Ribatski, J.R. Thome, Two-phase flow patterns and flow-pattern maps: Fundamentals and applications, Appl. Mech. Rev. 61 (5) (2008) 050802, http://dx.doi.org/10.1115/1.2955990, URL https://asmedigitalcollection.asme.org/appliedmechanicsreviews/article/doi/10.1115/1.2955990/446407/TwoPhase-Flow-Patterns-and-FlowPattern-Maps.

[30] J. Pettersen, Flow vaporization of CO_2 in microchannel tubes, Experimental Thermal and Fluid Science, Exp. Therm Fluid Sci. 28 (2) (2004) 111–121, http://dx.doi.org/10.1016/S0894-1777(03)00029-3, URL https://www.sciencedirect.com/science/article/pii/S0894177703000293.

[31] J. Pettersen, Two-phase flow patterns in microchannel vaporization of CO_2 at near critical pressure, Heat Transf. Eng. 25 (3) (2004) 52–60, http://dx.doi.org/10.1080/01457630490280100, URL http://www.tandfonline.com/doi/abs/10.1080/01457630490280100.

[32] R. Yun, Y. Kim, Flow regimes for horizontal two-phase flow of CO_2 in a heated narrow rectangular channel, Int. J. Multiph. Flow. 30 (10) (2004) 1259–1270, http://dx.doi.org/10.1016/j.ijmultiphaseflow.2004.07.003, URL https://linkinghub.elsevier.com/retrieve/pii/S0301932204001077.

[33] A.-E. Schael, M. Kind, Flow pattern and heat transfer characteristics during flow boiling of CO_2 in a horizontal micro fin tube and comparison with smooth tube data, Int. J. Refrig. 28 (8) (2005) 1186–1195, http://dx.doi.org/10.1016/j.ijrefrig.2005.09.002, URL https://linkinghub.elsevier.com/retrieve/pii/S0140700705001696.

[34] J.L. Gasche, Carbon dioxide evaporation in a single microchannel, J. Braz. Soc. Mech. Sci. Eng. 28 (1) (2006) 69–83, http://dx.doi.org/10.1590/S1678-58782006000100008, URL http://www.scielo.br/scielo.php?script=sci_arttext&pid=S1678-58782006000100008&lng=en&nrm=iso&tlng=en.

[35] J.R. Thome, G. Ribatski, State-of-the-art of two-phase flow and flow boiling heat transfer and pressure drop of CO_2 in macro- and micro-channels, Int. J. Refrig. 28 (8) (2005) 1149–1168, http://dx.doi.org/10.1016/j.ijrefrig.2005.07.005, URL https://linkinghub.elsevier.com/retrieve/pii/S0140700705001672.

[36] J.R. Thome, J.E. Hajal, Two-phase flow pattern map for evaporation in horizontal tubes: Latest version, Heat Transf. Eng. 24 (6) (2003) 3–10, http://dx.doi.org/10.1080/714044410, URL http://www.tandfonline.com/doi/abs/10.1080/714044410.

[37] VDI (Ed.), VDI Heat Atlas, 2nd ed., in: VDI-Buch, Springer, Berlin, New York, 2010, http://dx.doi.org/10.1007/978-3-540-77877-6.

[38] L. Cheng, G. Ribatski, L. Wojtan, J.R. Thome, New flow boiling heat transfer model and flow pattern map for carbon dioxide evaporating inside horizontal tubes, Int. J. Heat Mass Transfer 49 (21–22) (2006) 4082–4094, http://dx.doi.org/10.1016/j.ijheatmasstransfer.2006.04.003, URL https://linkinghub.elsevier.com/retrieve/pii/S0017931006002444.

[39] L. Cheng, G. Ribatski, L. Wojtan, J.R. Thome, Erratum to: "New flow boiling heat transfer model and flow pattern map for carbon dioxide evaporating inside horizontal tubes", Int. J. Heat Mass Transfer 50 (21–22) (2007) 391.

[40] L. Cheng, G. Ribatski, J. Moreno Quibén, J.R. Thome, New prediction methods for CO_2 evaporation inside tubes: Part I – A two-phase flow pattern map and a flow pattern based phenomenological model for two-phase flow frictional pressure drops, Int. J. Heat Mass Transfer 51 (1–2) (2008) 111–124, http://dx.doi.org/10.1016/j.ijheatmasstransfer.2007.04.002, URL https://linkinghub.elsevier.com/retrieve/pii/S0017931007002839.

[41] R. Mastrullo, A.W. Mauro, J.R. Thome, D. Toto, G.P. Vanoli, Flow pattern maps for convective boiling of CO_2 and R410A in a horizontal smooth tube: Experiments and new correlations analyzing the effect of the reduced pressure, Int. J. Heat Mass Transfer 55 (5) (2012) 1519–1528, http://dx.doi.org/10.1016/j.ijheatmasstransfer.2011.11.003, URL https://www.sciencedirect.com/science/article/pii/S0017931011006405.

[42] L. Cheng, G. Xia, J.R. Thome, Flow boiling heat transfer and two-phase flow phenomena of CO_2 in macro- and micro-channel evaporators: Fundamentals, applications and engineering design, Appl. Therm. Eng. 195 (2021) 117070, http://dx.doi.org/10.1016/j.applthermaleng.2021.117070, URL https://linkinghub.elsevier.com/retrieve/pii/S1359431121005147.

[43] P.A. Kew, K. Cornwell, Correlations for the prediction of boiling heat transfer in small-diameter channels, Appl. Therm. Eng. 17 (8–10) (1997) 705–715, http://dx.doi.org/10.1016/S1359-4311(96)00071-3, URL https://linkinghub.elsevier.com/retrieve/pii/S1359431196000713.

[44] S.G. Kandlikar, Fundamental issues related to flow boiling in minichannels and microchannels, Exp. Therm Fluid Sci. 26 (2–4) (2002) 389–407, http://dx.doi.org/10.1016/S0894-1777(02)00150-4, URL https://linkinghub.elsevier.com/retrieve/pii/S0894177702001504.

[45] C.L. Ong, J.R. Thome, Macro-to-microchannel transition in two-phase flow: Part 1 – Two-phase flow patterns and film thickness measurements, Exp. Therm Fluid Sci. 35 (1) (2011) 37–47, http://dx.doi.org/10.1016/j.expthermflusci.2010.08.004, URL https://linkinghub.elsevier.com/retrieve/pii/S0894177710001500.

[46] V. Bhanot, L. Zwalinski, J. Noite, H. Postema, J. Godlewski, T. Köttig, B. Verlaat, The CORA CO_2 cooling plant, in: 10th IIF/IIR Gustav Lorentzen Conference on Natural Working Fluids, GL-239, Delft, The Netherlands, 2012.

[47] M. Ritzert, E. Blanco Viñuela, M. Ostrega, L. Zwalinski, UNICOS framework and EPICS: A possible integration, in: Proceedings of the 16th Int. Conf. on Accelerator and Large Experimental Control Systems, ICALEPCS2017, JACoW, Barcelona, Spain, ISBN: 978-3-95450-193-9, 2018, http://dx.doi.org/10.18429/JACOW-ICALEPCS2017-TUPHA201.

[48] M. Huber, A. Harvey, E. Lemmon, G. Hardin, I. Bell, M. McLinden, NIST Reference Fluid Thermodynamic and Transport Properties Database (REFPROP) Version 10 - SRD 23, National Institute of Standards and Technology, 2018, http://dx.doi.org/10.18434/T4/1502528, type: dataset, URL https://www.nist.gov/srd/refprop.

[49] X. Fu, P. Zhang, H. Hu, C.J. Huang, Y. Huang, R.Z. Wang, 3D visualization of two-phase flow in the micro-tube by a simple but effective method, J. Micromech. Microeng. 19 (8) (2009) 085005, http://dx.doi.org/10.1088/0960-1317/19/8/085005, URL https://iopscience.iop.org/article/10.1088/0960-1317/19/8/085005.

[50] R. Revellin, V. Dupont, T. Ursenbacher, J.R. Thome, I. Zun, Characterization of diabatic two-phase flows in microchannels: Flow parameter results for R-134a in a 0.5 mm channel, Int. J. Multiph. Flow. 32 (7) (2006) 755–774, http://dx.doi.org/10.1016/j.ijmultiphaseflow.2006.02.016, URL https://linkinghub.elsevier.com/retrieve/pii/S0301932206000541.

[51] H. Wu, Q. Duan, Gas void fraction measurement of gas-liquid two-phase CO_2 flow using laser attenuation tehnique, Sensors 19 (14) (2019) 3178, http://dx.doi.org/10.3390/s19143178, URL https://www.mdpi.com/1424-8220/19/14/3178.

[52] K. He, X. Zhang, S. Ren, J. Sun, Deep residual learning for image recognition, 2015, URL http://arxiv.org/abs/1512.03385, arXiv:1512.03385 [cs].

[53] J.R. Thome, Wieland-Werke, The Heat Transfer Data Book III Enhanced Heat Transfer Design Methods for Tubular Heat Exchangers, 2016, OCLC: 962096023, URL https://nbn-resolving.org/urn:nbn:de:101:1-201610183373.

[54] J.R. Thome, A. Cioncolini, Encyclopedia of Two-Phase Heat Transfer and Flow I: Fundamentals and Methods Volume 3: Flow Boiling in Macro and Microchannels, Vol. 3, World Scientific, 2015, http://dx.doi.org/10.1142/9310-vol3, URL https://www.worldscientific.com/worldscibooks/10.1142/9310-vol3,

[55] Y. Taitel, D. Barnea, A.E. Dukler, A film model for the prediction of flooding and flow reversal for gas-liquid flow in vertical tubes, Int. J. Multiph. Flow. 8 (1) (1982) 1–10, http://dx.doi.org/10.1016/0301-9322(82)90002-7, URL https://linkinghub.elsevier.com/retrieve/pii/0301932282900027.

[56] D. Barnea, Y. Taitel, Stability of annular flow, Int. Commun. Heat Mass Transfer 12 (5) (1985) 611–621, http://dx.doi.org/10.1016/0735-1933(85)90084-3, URL https://linkinghub.elsevier.com/retrieve/pii/0735193385900843.

[57] J. Weisman, S. Kang, Flow pattern transitions in vertical and upwardly inclined lines, Int. J. Multiph. Flow. 7 (3) (1981) 271–291, http://dx.doi.org/10.1016/0301-9322(81)90022-7, URL https://linkinghub.elsevier.com/retrieve/pii/0301932281900227.

[58] H. Mukherjee, J.P. Brill, Empirical equations to predict flow patterns in two-phase inclined flow, Int. J. Multiph. Flow. 11 (3) (1985) 299–315, http://dx.doi.org/10.1016/0301-9322(85)90060-6, URL https://linkinghub.elsevier.com/retrieve/pii/0301932285900606.

[59] S. Jayanti, G. Hewitt, Prediction of the slug-to-churn flow transition in vertical two-phase flow, Int. J. Multiph. Flow. 18 (6) (1992) 847–860, http://dx.doi.org/10.1016/0301-9322(92)90063-M, URL https://linkinghub.elsevier.com/retrieve/pii/030193229290063M.

[60] X.T. Chen, J. Brill, Slug to churn transition in upward vertical two-phase flow, Chem. Eng. Sci. 52 (23) (1997) 4269–4272, http://dx.doi.org/10.1016/S0009-2509(97)00178-4, URL https://linkinghub.elsevier.com/retrieve/pii/S0009250997001784.

[61] S. Lips, J.P. Meyer, Experimental study of convective condensation in an inclined smooth tube. Part I: Inclination effect on flow pattern and heat transfer coefficient, Int. J. Heat Mass Transfer 55 (1–3) (2012) 395–404, http://dx.doi.org/10.1016/j.ijheatmasstransfer.2011.09.033, URL https://linkinghub.elsevier.com/retrieve/pii/S0017931011005382.

[62] T. Layssac, S. Lips, R. Revellin, Experimental study of flow boiling in an inclined mini-channel: Effect of inclination on flow pattern transitions and pressure drops, Exp. Therm Fluid Sci. 98 (2018) 621–633, http://dx.doi.org/10.1016/j.expthermflusci.2018.07.004, URL https://linkinghub.elsevier.com/retrieve/pii/S0894177718305843.

[63] X. Fang, Q. Wu, Y. Yuan, A general correlation for saturated flow boiling heat transfer in channels of various sizes and flow directions, Int. J. Heat Mass Transfer 107 (2017) 972–981, http://dx.doi.org/10.1016/j.ijheatmasstransfer.2016.10.125, URL https://linkinghub.elsevier.com/retrieve/pii/S0017931016313953.

[64] D. Hellenschmidt, M. Bomben, G. Calderini, M. Boscardin, M. Crivellari, S. Ronchin, P. Petagna, New insights on boiling carbon dioxide flow in mini- and micro-channels for optimal silicon detector cooling, Nucl. Instrum. Methods Phys. Res. A 958 (2020) 162535, http://dx.doi.org/10.1016/j.nima.2019.162535, URL https://linkinghub.elsevier.com/retrieve/pii/S0168900219310654.